Rupture Characteristics and Bedrock Structural Control of the 2016 M_w 6.0 Intraplate Earthquake in the Petermann Ranges, Australia

Januka Attanayake[*1], Tamarah R. King[1,2], Mark C. Quigley[1], Gary Gibson[1], Dan Clark[3], Abraham Jones[1], Sarah L. Brennand[2,4], and Mike Sandiford[1]

ABSTRACT

The 20 May 2016 surface-rupturing intraplate earthquake in the Petermann Ranges is the largest onshore earthquake to occur in the Australian continent in 19 yr. We use in situ and Interferometric Synthetic Aperture Radar surface observations, aftershock distribution, and the fitting of *P*-wave source spectra to determine source properties of the Petermann earthquake. Surface observations reveal a 21-km-long surface rupture trace (strike = 294° ± 29°) with heterogeneous vertical displacements (< 0.1–0.96 m). Aftershock arrays suggest a triangular-shaped rupture plane (dip ≈ 30°) that intersects the subsurface projection of the major geophysical structure (Woodroffe thrust [WT]) proximal to the preferred location of the mainshock hypocenter, suggesting the mainshock nucleated at a fault junction. Footwall seismicity includes apparent southwest-dipping Riedel-type alignments, including possible activation of the deep segment of the WT. We estimate a moment magnitude (M_w) of 6.0 and a corner frequency (f_c) of 0.2 Hz, respectively, from spectral fitting of source spectra in the 0.02–2 Hz frequency band. These translate into a fault area of 124 km^2 and an average slip of 0.36 m. The estimated stress drop of 2.2 MPa is low for an intraplate earthquake; we attribute this to low-frictional slip (effective coefficient of friction > 0.015) along rupture-parallel phyllosilicate-rich surfaces within the host rock fabric with possible additional contributions from elevated pore-fluid pressures.

KEY POINTS

- The 2016 Petermann Ranges earthquake is the largest onshore event in Australia in nearly 20 yr.
- The low-stress drop event (2.2 MPa) was on a weak fault aligned with older phyllosilicate-rich surfaces.
- The earthquake may have nucleated at the junction of the northeast-dipping source fault and the Woodroffe thrust.

INTRODUCTION

Continental intraplate earthquakes can cause disproportionately more damage than their interplate equivalents (Bilham, 2014), and regardless of tectonic domains, the fault displacement hazard earthquakes pose may increase when accompanied by surface rupture (e.g., Yifan, 2008). Obtaining accurate measures of the dimensions, geometry, and slip of fault ruptures are important for comparative analysis of seismic moment estimates, refining source-moment scaling relationships (Leonard, 2010) and seismic hazard analyses (Allen *et al.*, 2018). The 20 May 2016 Petermann Ranges earthquake (hereafter referred as Petermann earthquake) is the largest onshore earthquake recorded in the Australian continent in 19 yr, with an estimated magnitude ranging from M_w 5.9 to 6.1 based on different data and modeling approaches (Geoscience Australia, Polcari *et al.*, 2018; Hejrani and Tkalčić, 2019). The remote location of the earthquake resulted in no damage or loss of life. In this study, we integrate field and remotely sensed observations of surface faulting and deformation, aftershock distribution, and source spectrum analysis to determine fault dimensions, geometry, and rupture characteristics (e.g., average slip and stress drop) of the Petermann earthquake. Our results reduce nonuniqueness in source parameters estimated in previous studies. We also present evidence for (1) subparallelism between bedrock fabrics and rupture orientation, and (2) spatial associations between

1. School of Earth Sciences, University of Melbourne, Parkville, Victoria, Australia; 2. Now at Department of Earth Sciences, University of Oxford, Oxford, United Kingdom; 3. Geoscience Australia, Symonston, ACT, Australia; 4. Now at University of Queensland, Brisbane, Queensland, Australia

*Corresponding author: januka.attanayake@unimelb.edu.au

Cite this article as Attanayake, J., T. R. King, M. C. Quigley, G. Gibson, D. Clark, A. Jones, S. L. Brennand, and M. Sandiford (2020). Rupture Characteristics and Bedrock Structural Control of the 2016 M_w 6.0 Intraplate Earthquake in the Petermann Ranges, Australia, *Bull. Seismol. Soc. Am.* **110**, 1037–1045, doi: 10.1785/0120190266

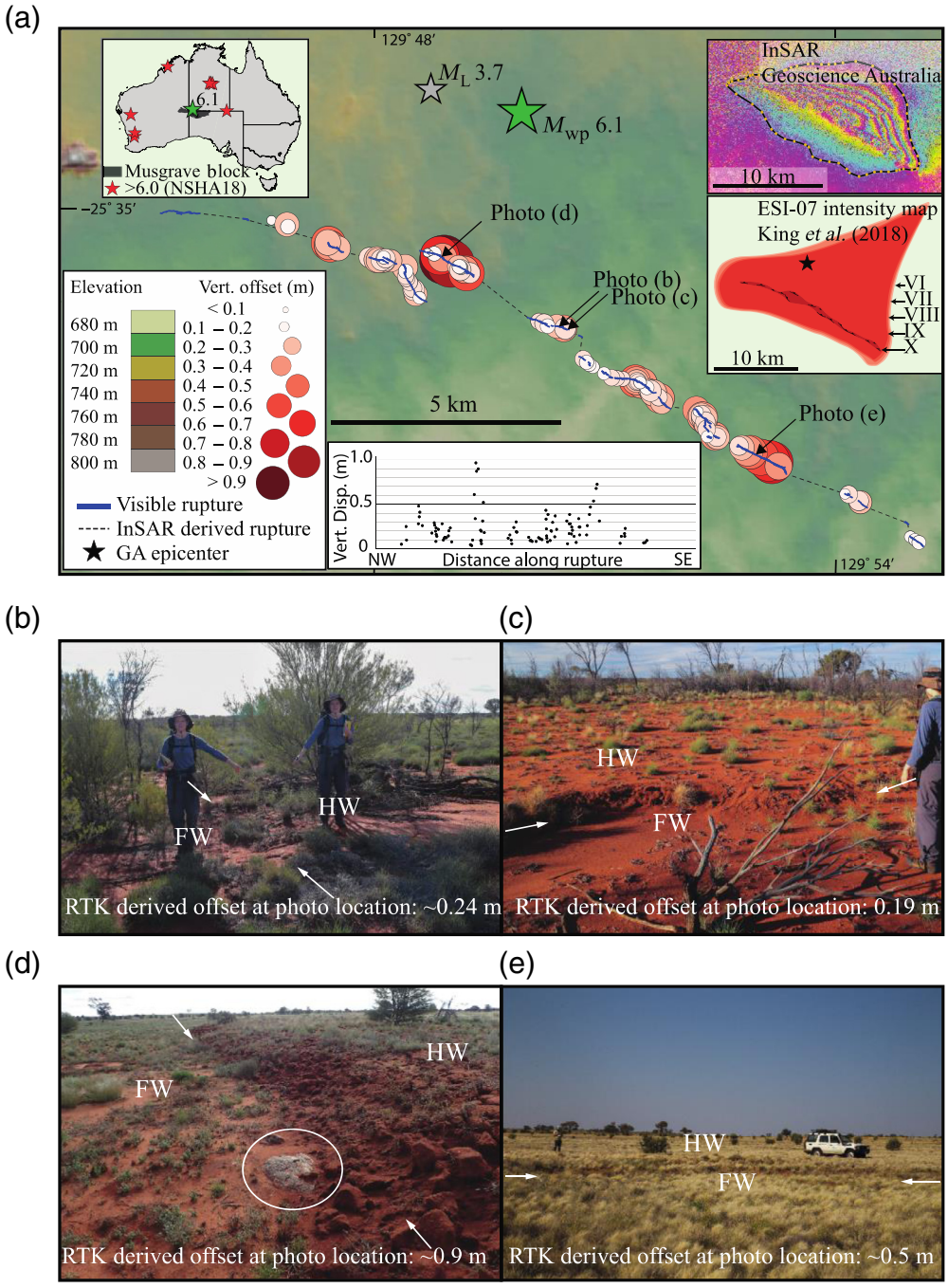

Figure 1. Surface observations of the 2016 Petermann thrust (PT) surface rupture. (a) Map showing: the surface trace of both Interferometric Synthetic Aperture Radar (InSAR) defined rupture, and where rupture is observable at the surface; real time kinematic (RTK)-derived vertical offset measurements are shown as red circles scaled to the magnitude of offset; the epicenters of the main and main aftershock events as green and gray stars, respectively; locations of photos. Inset maps show: the locations of $M_w > 6.0$ since 1910 and the outline of the Musgrave block; InSAR for the Petermann earthquake; and ESI-07 contours as described in King *et al.* (2018). In situ RTK measurements along the strike are also shown. (b–e) Photos demonstrating variation in offset and morphology of the surface rupture, with white arrows pointing along the bottom of the rupture, labels indicating the hanging wall and footwall, and vertical offset from RTK measurements closest to the photo locations. Photos (b) and (c) were taken 20 days after the mainshock near the middle of the surface rupture. Photos (d) and (e) were taken 16 months after the mainshock, in the vicinity of the largest vertical offset measurements. The exposed basement rock outcrop circled in (d) has foliations oriented parallel to the arrows showing the surface rupture. ESI, environmental seismic intensity; FW, footwall; GA, Geoscience Australia; HW, hanging wall; NSHA18, National Seismic Hazard Analysis (Allen *et al.*, 2018); Vert. Disp., vertical displacement. The color version of this figure is available only in the electronic edition.

fault intersections, hypocenter location, and aftershock activity. Collectively these provide evidence for an influence of crustal geological structure on the rupture dynamics of the Petermann earthquake.

SEISMOTECTONICS

Australia has experienced nine onshore events $M_w > 6.0$ since 1910 (Fig. 1a, Allen *et al.*, 2018) and averages two $M_w > 5$ events per year (Leonard, 2008). Nine surface-rupturing earthquakes with $4.7 \le M_w \le 6.6$ (including the one investigated here) have been reported since 1968 (Clark *et al.*, 2014). Most $M_w > 5.5$ historic events have occurred in remote cratonic Australia and caused no fatalities. However, hundreds of faults with potential neotectonic movement have been identified across the continent (Quigley *et al.*, 2006; Clark *et al.*, 2012), and the full historic earthquake catalog highlights four zones of high seismicity (Leonard, 2008; Allen *et al.*, 2018), three of which are close to major cities (Perth, Adelaide, and Melbourne).

The regional crustal stress field varies across the continent in response to distant Indo-Australian plate boundary forces (Coblentz *et al.*, 1998; Rajabi *et al.*, 2017). The Petermann earthquake occurred in the western Musgrave block (Fig. 1a), a Mesoproterozoic basement province (Edgoose *et al.*, 2004) near the Northern Territory, South Australia, and Western Australia border with an approximate orientation of maximum horizontal present-day stress (SH_{max}) of 043° (Rajabi *et al.*, 2017). The earthquake ruptured through granitic mylonites on the hanging wall

of the southwest-dipping Woodroffe thrust (WT), a major structure which controlled lower-crustal uplift and metamorphism during the 580–520 Ma Petermann orogeny (Edgoose *et al.*, 2004). The WT location and geometry is defined by regional geophysical maps (Edgoose *et al.*, 2004; Raimondo *et al.*, 2010) and seismic reflection profiles (Neumann, 2013). The mapped trace of the WT is approximately 10 (±3) km north of the surface rupture trace created by the Petermann earthquake, dips approximately 30° (±10°) southwest (Neumann, 2013) and may be up to 3 (±1) km wide (Camacho *et al.*, 1995; Edgoose *et al.*, 2004; Raimondo, 2010).

The large gravity anomalies (~150 mGal) observed in this region were produced by Alice Springs (300–450 Ma) and Petermann (500–550 Ma) orogenies, and they appear to reflect lithospheric strength (Beekman *et al.*, 1997; Sandiford, 2002). The Petermann orogen is a large zone of deformation having dimensions of ~1500 km (east–west) and ~300 km (north–south) with an estimated north–south shortening exceeding 100 km, and possibly sustained a deformation rate of about 1.5–2 mm/yr over a 50–60 Ma period (Flöttmann *et al.*, 2004; Raimondo *et al.*, 2010). Although the WT appears to have accommodated a substantial part of this deformation, a precise estimate of the deformation rate is still lacking. Moreover, a clear relationship between the present-day gravitational anomalies and brittle deformation associated with this broad deformation zone is yet to be established (Copley, 2017).

RUPTURE CHARACTERISTICS

Surface observations

Interferometric Synthetic Aperture Radar (InSAR) displacement fringes (Fig. 1a) and differenced digital elevation models (dDEMs) for the Petermann earthquake highlight an approximately 21-km-long surface rupture with a 7-km-wide zone of hanging-wall deformation and <3-km-wide zone of footwall deformation (Polcari *et al.*, 2018; Gold *et al.*, 2019). The zone of observed environmental damage is wider on the hanging wall compared with the footwall (Fig. 1a). Along the 21 km rupture trace defined by InSAR, visible fault offset at the surface is discontinuous and highly variable in intensity and morphology (Fig. 1b–e). The overall rupture has a slightly convex shape (relative to the epicenter), with strike deviating from ~280° in the northwest to ~303° in the southeast. We therefore describe the average fault strike as 294° ± 29°, derived from averages of the InSAR (288° ± 33°) and observable surface rupture traces (299° ± 25°).

High-accuracy elevation measurements along the visible surface rupture were obtained 5 weeks after the mainshock using a real time kinematic (RTK) Global Positioning System (see Data and Resources). From the RTK measurements, 104 vertical offset measurements were derived across the hanging wall and footwall (Fig. 1a). From the RTK data, average vertical offset along the rupture is just 0.23 m, with a standard deviation ±0.18 m and median of 0.18 m. Maximum vertical offset of 0.96 m occurs approximately 8 km (from the northwesternmost point) along the rupture (close to Fig. 1d). Within 180 m either side of this maximum value, vertical offset diminishes to <0.1 m. The second highest vertical offset of 0.72 m occurs 17 km along the rupture (close to Fig. 1e) and decreases to <0.3 m within 600 m either side. These vertical measurements may underestimate actual fault displacement, because they do not capture distributed deformation away from the surface rupture and lateral slip components.

Aftershock distribution

Beginning three days after the Petermann earthquake, Geoscience Australia and the University of Melbourne started installing a temporary seismic network of nine stations in the vicinity of the main earthquake. From the data recorded by these stations, we precisely located 69 events with $-0.2 \le M_L \le 3.5$ using the eqFocus software (Attanayake *et al.*, 2019). In this method, we handpicked *P*- and *S*-phase arrivals, computed travel-time predictions using a local velocity model (TC1A, see Data and Resources), and handled the inversion using the Levenberg–Marquardt minimization procedure. Owing to the distance to the nearest station being smaller than the hypocentral depth, the average depth uncertainty is only ±0.37 km in this dataset (see Data and Resources). The distribution of these aftershocks is shown in Figure 2a. It is evident that aftershocks located east of the surface trace define a fault plane with an average dip of ~30° to the northeast (Fig. 2b). Activity on this fault plane appears to be contained within the uppermost 7 km of the crust. The depth to the fault below the epicenter of the main earthquake is ~3 km, consistent with the shallow centroid depth estimated in previous studies (e.g., Hejrani and Tkalčić, 2019). The aftershocks located west of the surface trace appear to align with the projected plane of the WT that dips to the southwest. The Petermann earthquake epicenter overlies the intersection of the projected WT and the Petermann aftershock lineament; this spatial overlap suggests the possibility that the Petermann earthquake nucleated proximal to or within this fault junction zone, as observed for many crustal earthquakes (Gabrielov *et al.*, 1996; Talwani, 1999; Quigley *et al.*, 2019). Another intriguing observation is the sets of southwest-dipping aftershock arrays parallel to the WT, but deeper within the footwall of the Petermann earthquake source fault (Fig. 2b); the ~30° counter-clockwise orientation with respect to the Petermann fault is consistent with the expected orientations of early en échelon Riedel shears (Tchalenko, 1970).

Fitting moment rate spectral density functions

We performed *P*-wave source spectral modeling to determine the moment (M_0) and stress drop ($\Delta\sigma$) of the Petermann earthquake. To begin with, all openly available teleseismic ($30° \le \Delta \le 90°$ *P* waveforms (324 in total) for this earthquake were downloaded for processing (see Data and Resources). After decimating sampling period to 0.05 s, we deconvolved

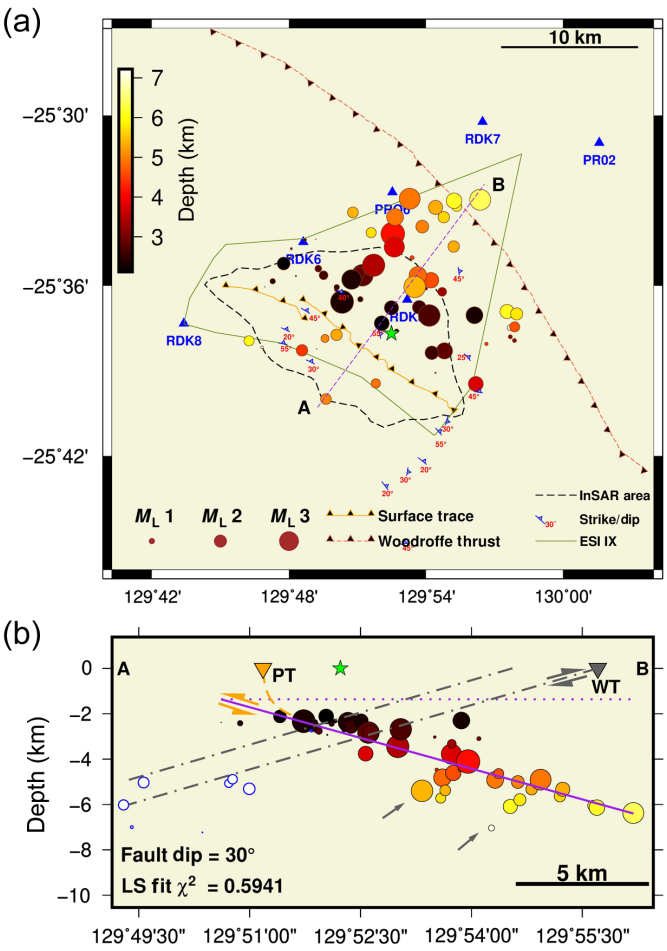

Figure 2. Distribution of aftershocks. (a) Map showing the aftershock distribution (solid circles) shaded by depth along with the surface trace of the Petermann Ranges earthquake (PT) and the Woodroffe thrust (WT). The epicenter of the main event from the International Seismological Centre (ISC) catalog is shown by the star (see Data and Resources). Six temporary seismic stations are also shown (triangles), whereas the other three stations are out of the field of view. The depth of aftershocks located to the east of the PT increases to the northeast. The ESI level IX is represented by the solid line (King *et al.*, 2018). The strike and dip of foliation is from Scrimgeour *et al.* (1999). The area outlined in Figure 1 of deformation detected by InSAR image is outlined by dashed lines. (b) The aftershocks projected on to a cross section along the AB profile shown in (a), which is approximately orthogonal to the average strike of the PT. The solid line is fitted to aftershocks using a least-squares (LS) method, from which the fault dip (30°) is estimated (the dotted line is horizontal). The reduced χ^2 for the least-squares fit is also given. The inverted triangles show the surface intersections of the PT and WT. The dashed line extending the PT from the surface is arbitrarily drawn to connect with the underlying fault plane. The white circles are aftershocks located west of the PT. They align with the projected fault plane of the ~3-km-wide WT (dashed–dotted lines) with a dip of 20°, but the dip could vary between 20° and 30° (Stewart, 1995; Neumann, 2013). The small arrows point to possible Riedel shears in the footwall delineated by aftershocks. The color version of this figure is available only in the electronic edition.

the instrument response to obtain displacement waveforms. An automatic signal-to-noise ratio (SNR) filter was applied to quality control data, for which root mean square (rms) of ±5 s around the peak of the *P* wave detected using the theoretical arrival time predicted from the ak135 reference Earth model (Montagner and Kennett, 1995) was computed as the signal amplitude and the rms of 10 s preceding this time window was computed as the noise amplitude. Following this procedure, data with SNR ≥ 5 were selected for further analysis. We also removed data with gaps, ending up with 120 azimuthally distributed high-quality seismograms for modeling (Fig. 3a). We then handpicked precise *P*-wave arrival times (T_P) and assigned 8 s proceeding T_P to the signal window and 8 s preceding T_P to the noise window. This windowing ensures that the entire first arrival *P* waveform is captured and that it is the dominant wave within the signal window.

We computed moment rate spectral density functions (MRSDFs) as given in equation (1) (Houston and Kanamori, 1986) using these 120 displacement *P* waveforms between 0.02 and 2 Hz (Fig. 3b). In this frequency band, the signal is well separated from noise, whereas a higher cutoff frequency results in poor signal–noise separation because the power of noise approaches that of the signal at frequencies greater than 2 Hz.

$$\mathrm{MRSDF} = \frac{4\pi\rho\alpha^3 E_R}{G(\Delta)C(\Delta)R(s,d,r)}\exp[\pi f t^*]D(f), \qquad (1)$$

in which ρ and α are, respectively, density (2608 kg/m^3) and *P*-wave velocity (5.56 km/s) of the medium at the hypocenter obtained from the Australian Reference Earth Model (AuSREM) reference model (Salmon *et al.*, 2013). E_R is the radius of the Earth (6371 km). $G(\Delta)$ and $C(\Delta)$ are geometric spreading and free-surface amplification corrections based on the ak135 model (Fig. 4a,b), for which equations are given by Kanamori and Stewart (1976) and Bullen and Bolt (1985), respectively. R is the radiation pattern correction (Aki and Richards, 2009), which depends on strike (s, 294°), dip (d, 30°), and rake (r, we assumed a pure thrust fault with $r = 90°$ based on our in situ observations) of the fault plane. $D(f)$ is the Fourier transform of the displacement *P* waveform. Finally, we used teleseismic t^* model of Choy and Cormier (1986), as given in the following equation to correct for frequency (f)-dependent attenuation:

$$t^* = \begin{cases} 0.9 - 0.1\times\log(f) & f < 0.1 \text{ Hz} \\ 0.5 - 0.5\times\log(f) & 0.1 \le f < 1.0 \text{ Hz} \\ 0.5 - 0.1\times\log(f) & 1.0 \le f \text{ Hz} \end{cases}. \qquad (2)$$

After computing individual MRSDFs, we averaged them logarithmically to obtain a representative MRSDF of the Petermann earthquake (Fig. 4b, left panel). This averaging ensures that unmodeled site, path, and radiation effects and the trade-off between the corner frequency (f_c) and the spectral fall-off rate (n) are minimized (Houston and Kanamori, 1986; Kaneko and Shearer, 2014).

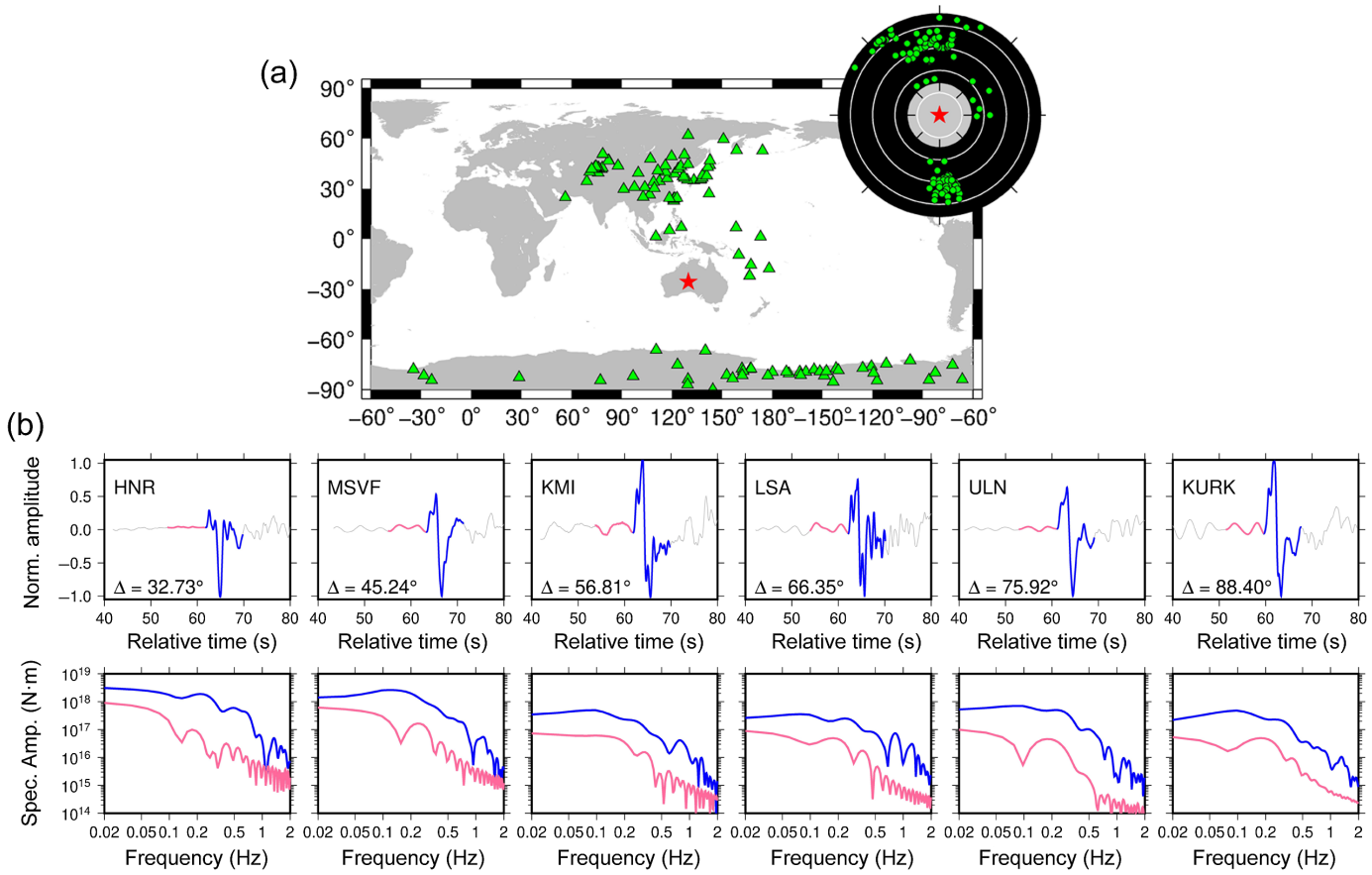

Figure 3. (a) Spatial distribution of the 120 teleseismic stations (triangles) from which data are selected to compute moment rate spectral density functions (MRSDFs). The star is the epicenter of the earthquake. The inset polar plot shows the azimuthal and distance distribution of these stations, where the radial axis (distance) varies from 0° at the center to 90° at the circumference with a contour interval of 20°. (b) Top panel: Typical examples of 16-s-long time windows of signal (8 s, darker shade) and noise (8 s, lighter shade) for each decade of distance (thinnest line is the longer seismogram for perspective). The station name and the distance is also shown. Bottom panel: Corresponding MRSDFs computed for signal (darker shade) and noise windows (lighter shade). Noise is well separated from the signal between 0.02 and 2 Hz. The color version of this figure is available only in the electronic edition.

We then fit theoretical source spectral model of Boatwright (1978) (equation 3) to the average MRSDF to estimate M_0 and f_c through a grid-search procedure similar to that of Kaneko and Shearer (2014) with a grid sampling of 0.1 for M_w, f_c, and n. The best-fitting parameters are obtained by minimizing the frequency-normalized rms value between the observed MRSDF and the theoretical one.

$$\Omega(f) = \frac{M_0}{(1 + (\frac{f}{f_c})^{2\gamma})^{\frac{1}{2}}}, \tag{3}$$

in which $\Omega(f)$ is the theoretical MRSDF, M_0 is the long-period spectral asymptote equivalent to the moment that scales with moment magnitude (M_w), and γ is a fitting parameter. We prefer the model of Boatwright (1978) to the more commonly used Brune (1970) one (i.e., $\gamma = 1$) because fit to spectra at frequencies greater than f_c is better with Boatwright's theory in general (Kaneko and Shearer, 2014).

After estimating f_c, we use the relationships given by radially expanding singular crack model of Eshelby (1957) to estimate $\Delta\sigma$ (see the following equations):

$$F_r = k\frac{V_s}{f_c}, \tag{4}$$

$$\Delta\sigma = \left(\frac{7}{16}\right)\left(\frac{M_0}{F_r^3}\right). \tag{5}$$

In the previous equations, F_r is the fault radius and k is a proportionality constant relating F_r to shear velocity (V_S = 3.3 km/s, Salmon *et al.*, 2013) at the hypocenter and f_c. In our calculations, we used $k = 0.38$ assuming a rupture velocity of 0.9 V_S. This choice of k is based on the 3D cohesive zone dynamic circular rupture model of Kaneko and Shearer (2014). Our best-fitting estimates of source spectral parameters are summarized in Figure 4b ($M_0 = 1.2735 \times 10^{18}$ N · m, M_w 6.0, f_c = 0.2 Hz, n = 2.7). Using equations (4) and (5), we estimate fault area (πF_r^2) and stress drop to be 124 km^2 and 2.2 MPa, respectively. To estimate the 80% confidence interval of source parameters, we use bootstrapping, for which 30% of the MRSDFs are randomly removed and replaced in

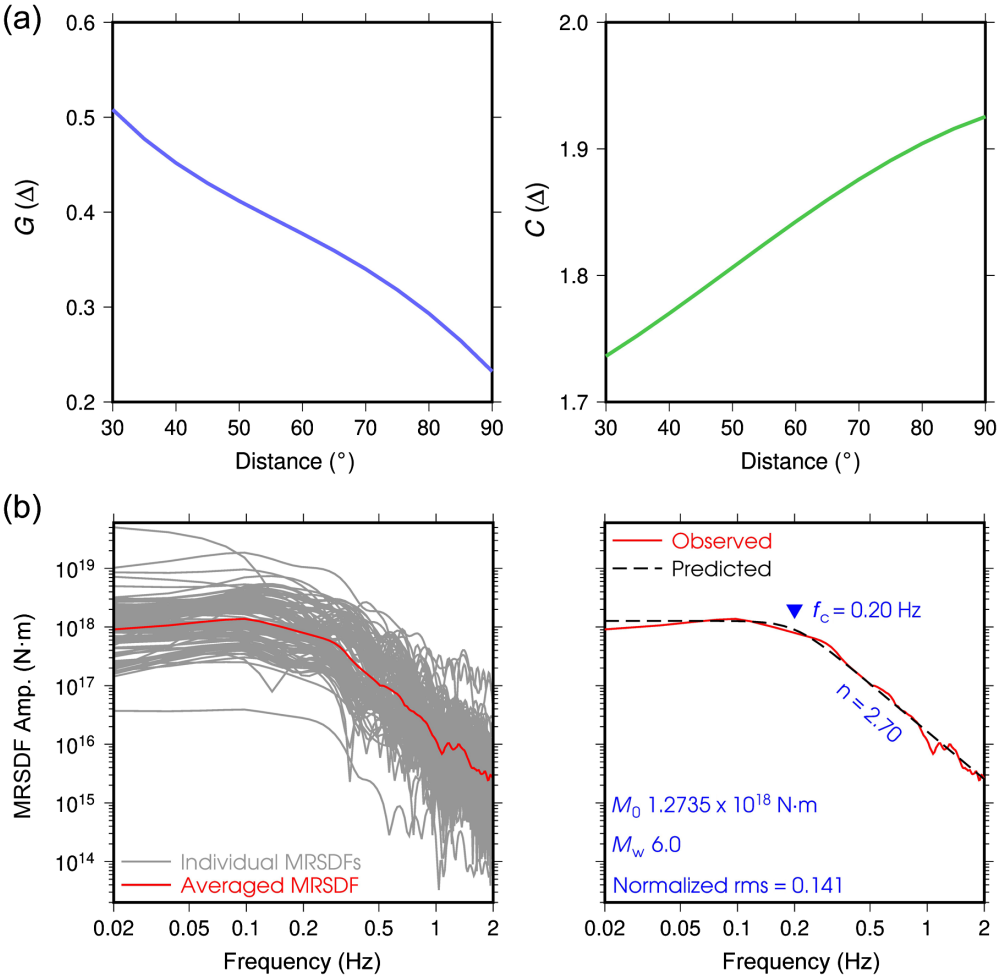

Figure 4. (a) Geometric spreading (G(Δ)) and free-surface amplification (C(Δ)) corrections as a function of distance. (b) Left panel: Individual MRSDFs and the logarithmically averaged representative MRSDF. Right panel: Theoretical MRSDF fitted to the representative MRSDF with the best-fitting corner frequency (f_c), fall-off rate (n), moment (M_0), moment magnitude (M_w), and frequency-normalized root mean square (rms) annotated. The color version of this figure is available only in the electronic edition.

1000 realizations. With this, the confidence interval for M_w, f_c, and n are [6.0, 6.1], [0.2, 0.3], and [2.4, 3.1], respectively.

DISCUSSION

The aftershock distribution provides key information regarding the geometry of the causative fault, for which least-squares fitting defines a plane dipping to the northeast with an angle of ~30° (Fig. 2b). This differs from the optimal dip angles reported in InSAR inversions of 39° (Polcari *et al.*, 2018) and 22° (Wang *et al.*, 2019) and the Global Centroid Moment Tensor (Global CMT) catalog estimate of 45°. Although these source inversions have produced variable dip angles possibly due to different data sensitivities, in situ measurements of rock foliations indicate an average dip angle ~25°–30° (Scrimgeour *et al.*, 1999, dip angles in Fig. 2a), lending confidence to our estimate. The environmental seismic intensity level IX contour in Figure 2a roughly encloses the active fault area defined by the aftershock distribution east of the surface trace. To a first order, the active fault area has a triangular shape with the ~21 km surface trace forming the base of the triangle and the height being the down-dip extent of aftershocks (~15 km). Using these dimensions, an independent estimate of approximate fault area can be obtained: $½ \times 21 \times 15 =$ ~158 km^2. In comparison, the estimate from fitting average MRSDF is 124 km^2 that independently validates the inferred source size within reasonable error bounds. If we used the fault area estimated from the aftershock distribution (158 km^2), stress drop reduces to 1.6 MPa.

Using M_w 6 and fault area 124 km^2, we estimate an average slip of 0.36 m for this rupture using the standard equation $M_0 = \mu A d$, in which M_0 is the seismic moment, μ is the dynamic shear modulus estimated from $\rho \times (V_S)^2$ at the source, A is the fault area, and d is the average slip. In this calculation, we used 2608 kg/m^3 and 3.3 km/s, respectively, for ρ and V_S from the AusREM model (Salmon *et al.*, 2013). The average slip of 0.36 m estimated here is consistent with an independent field-based average estimate of 0.42 m (King *et al.*, 2019) and an average estimate that is based on dDEMs of 0.4 ± 0.3 m over the entire length of the surface deformation zone (Gold *et al.*, 2019), particularly when considering the fact that the latter incorporates deformation partly attributable to coseismic warping and possible postseismic relaxation.

The source models inverted from InSAR measurements (Polcari *et al.*, 2018; Wang *et al.*, 2019) yield larger estimates of maximum slip (~1 m) and smaller fault areas (~45–75 km^2). It may be that the degree of heterogeneity of coseismic slip distribution as manifested in in situ surface displacement observations (King *et al.*, 2018; Gold *et al.*, 2019) are not fully captured in these inversions possibly, in part, due to smoothing and regularization procedures applied to achieve stability of solutions. Clearly, these models fall short of predicting

the down-dip extent of the active fault as apparent from the aftershock distribution.

The estimated $\Delta\sigma = 2.2$ MPa is significantly lower than the stress drop estimated for several well-recorded recent earthquakes in the Australian continent (20–50 MPa) (Dawson *et al.*, 2008; Attanayake *et al.*, 2019) and the global median for intraplate earthquakes of ~6 (±1) MPa (Allmann and Shearer, 2009). This lower $\Delta\sigma$ could be explained by a weak crust with low-differential stress (Hardebeck and Aron, 2009) and/or a low-friction rupture at shallow depths (Copley and Woodcock, 2016). On the one hand, western and central Australia are generally characterized by low-*Lg* wave attenuation (Wei *et al.*, 2017), high-predicted stress magnitudes (25–50 MPa; Coblentz *et al.*, 1998), and earthquakes with high stress drops (e.g., 27–53 MPa in M_w 4.7 Katanning earthquake in western Australia; Dawson *et al.*, 2008). Collectively these observations suggest high-crustal strength, eliminating weak crust as an explanation.

On the other hand, previous mapping (Camacho *et al.*, 1995; Scrimgeour *et al.*, 1999; Wex *et al.*, 2019) and our field observations of rupture-parallel, biotite mica-rich mylonitic layers in bedrock outcrops adjacent to the surface rupture (Fig. 1d) provide a plausible mechanism for low-friction faulting in the Petermann earthquake. The fact that these foliations do not align with the WT is an interesting observation, as the expectation is for them to be parallel to the WT. However, evidence for the presence of geologic fabrics that are dipping to the northeast and into the WT manifested as seismic reflectors in the uppermost crust is present in a recently reinterpreted seismic reflection profile about 175 km to the west of the epicentral region (seismic line 11GA-Y01, Neumann, 2013; de Gromard *et al.*, 2017). The putative geometry and orientation of these seismic reflectors resemble that observed of rupture parallel foliations in the epicentral region (see Data and Resources). Future structural geology research work on the morphology of the WT and origin of these foliations in the epicentral region could resolve geological processes that have produced the observed structural relationship between the WT and these foliations.

Intrinsic heterogeneities such as the presence of phyllosilicate-rich foliations and/or elevated pore pressures can reduce the frictional strength of faults, producing lower $\Delta\sigma$ (Collettini *et al.*, 2009; Copley, 2017). The mechanical behavior of phyllosilicate layers provides a fault weakening mechanism for generating lower $\Delta\sigma$ ruptures (Shea and Kronenberg, 1993). In addition, elevated pore pressures, possibly related to water-enhanced interlayers between less permeable phyllosilicate barriers, might also have played a role in fault weakening prior to or during rupture. Wang *et al.* (2019) proposed a correlation between seismicity and ground water level in the Petermann Ranges, but did not provide supporting evidence from the epicentral region nor propose a causal mechanism linking local hydrology with the Petermann rupture.

By assuming that estimated $\Delta\sigma$ represents a complete stress release, we compute the coefficient of friction (μ) of the Petermann fault—a proxy for fault strength. If, however, the Petermann earthquake released accumulated stress partially, this estimate is a lower bound to μ. We used the formulation of Suppe (2014) for computing $\mu : \sigma_1 - \sigma_3 = \kappa(\rho_r - \rho_w)gh$ and $\kappa = 2[\sin(\varphi) - \sin^2(\varphi)]$, in which $\varphi = a\tan(\mu)$. Here, $\sigma_1 - \sigma_3$ is the maximum differential stress ($= \Delta\sigma$), ρ_r and ρ_w are, respectively, the bulk density of the crust (2608 kgm^{-3}) and water (1000 kgm^{-3}), g is the gravitational acceleration (9.81 ms^{-2}), and h is hypocentral depth (1–5 km). μ is an effective value as we incorporate hydrostatic pore-fluid pressure in this computation, and our estimate is 0.015 ($h = 5$ km) $\leq \mu \leq 0.08$ ($h = 1$ km). This lower bound to μ is significantly less than widely used laboratory estimates (0.6–0.85) of Byerlee (1978), yet it is consistent with upper bounds to μ (0.02–0.24) estimated for intraplate reactivated thrust faults from regional scale force balance computations (Copley and Woodcock, 2016). Our low estimates of μ are also in accord with more recent rotary shear experimental predictions ($\mu \to 0$) at realistic slip rates (Di Toro *et al.*, 2004).

The alignment of deep footwall aftershocks with the projected WT (Fig. 2b) suggests localized seismic activation of this structure. Static and dynamic stress transfer (Freed, 2005) from the Petermann earthquake and/or other changes in fault structure or pore pressures might have been responsible for this observation. The triangular-shaped rupture plane intersects WT proximal to the preferred location of the Petermann earthquake hypocenter, suggesting the earthquake may have nucleated at this fault junction. Finally, the presence of apparent Riedel shears identified by short arrays of aftershocks in the footwall contributes to our understanding of the complex structural fabrics that may be created or reactivated and enhanced by crustal earthquakes. Further monitoring of seismicity in the source region may provide a better picture of these apparent pervasive footwall structures.

In conclusion, our study clearly indicates that the causative fault of the M_w 6 Petermann earthquake in 2016 was not located on the southwest-dipping WT, as proposed by de Gromard *et al.* (2019), but was located on a structurally controlled, anomalously weak intraplate fault dipping to the northeast and toward the WT, consistent with previous field observations and satellite data (King *et al.*, 2018; Polcari *et al.*, 2018; Gold *et al.*, 2019; Wang *et al.*, 2019).

DATA AND RESOURCES

The link to Geoscience Australia earthquake catalog is https://earthquakes.ga.gov.au/ (last accessed April 2019). The Global Centroid Moment Tensor (Global CMT) catalog can be found at https://www.globalcmt.org/CMTsearch.html (last accessed April 2019). Teleseismic *P* waveforms of the Petermann earthquake were downloaded from the Incorporated Research Institutes for Seismology (IRIS) Wilber 3 website https://ds.iris.edu/wilber3/find_event (last accessed March 2019). The in situ real time kinematic (RTK) vertical displacement measurements, TC1A crustal velocity model, information pertaining to the seismic profile line 11GA-Y01,

and the aftershock catalog are available at https://github.com/unimelb-geophys/Petermann-Ranges (last accessed August 2019). The International Seismological Centre (ISC) catalog can be accessed at http://www.isc.ac.uk/iscbulletin/search/ (last accessed March 2019). Ray tracing to compute radiation pattern, geometric spreading, and free-surface corrections were done with TauP Toolkit (Crotwell *et al.*, 1999). All figures except Figure 1 were made with Generic Mapping Tools, version 5.4.2 (v.5.4.2; Wessel *et al.*, 2013). The seismograms were preprocessed with Seismic Analysis Code (SAC; Goldstein *et al.*, 2003).

ACKNOWLEDGMENTS

The University of Melbourne's (UoM) temporary seismic array was funded by AuScope's Australian Geophysical Observing System (AGOS) Subsurface Observatory through an Education Investment Fund (EIF) grant. Geoscience Australia contributed data from four additional seismographs to the study. In addition, Geological Survey of South Australia (GSSA) contributed some equipment to the UoM temporary array. Mark C. Quigley is supported by the Australian Research Council through Discovery Grant Number DP170103350, and Tamarah R. King is supported through the Australian Government Research Training Program Scholarship. Dan Clark and Sarah L. Brennand publish with the permission of the CEO of Geoscience Australia. This article underwent two cycles of revision, during which Associate Editors Cezar Trifu and Mark Stirling along with three anonymous reviewers provided constructive comments.

REFERENCES

Aki, K., and P. G. Richards (2009). *Quantitative Seismology*, Second Ed., University Science Books, Mill Valley, California, 108 pp.

Allen, T., J. Griffin, M. Leonard, D. Clark, and H. Ghasemi (2018). The 2018 National Seismic Hazard Assessment for Australia: Model overview, *Geoscience Australia Record 2018/27*, Canberra, Australia, 126 pp., doi: 10.11636/Record.2018.027.

Allmann, B. P., and P. M. Shearer (2009). Global variations of stress drop for moderate to large earthquakes, *J. Geophys. Res.* **114,** no. B01310, doi: 10.1029/2008JB005821.

Attanayake, J., D. Sandiford, L. S. Schleicher, A. Jones, G. Gibson, and M. Sandiford (2019). Interacting intraplate fault systems in Australia: The Thorpdale, Victoria seismic sequences, *J. Geophys. Res.* doi: 10.1029/2018JB016945.

Beekman, F., R. A. Stephenson, and R. J. Korsch (1997). Mechanical stability of the Redbank Thrust Zone, Central Australia: Dynamic and rheological implications, *Aust. J. Earth Sci.* **44,** no. 2, 215–226.

Bilham, R. (2014). Aggravated earthquake risk in South Asia: Engineering versus human nature, in *Earthquake Hazard, Risk, 60 and Disasters*, M. Wyss (Editor), Elsevier, Amsterdam, The Netherlands, 103–141, doi: 10.1016/B978-0-12-394848-9.00005-5.

Boatwright, J. (1978). Detailed spectral analysis of two small New York State earthquakes, *Bull. Seismol. Soc. Am.* **68,** no. 4, 1117–1131.

Brune, J. N. (1970). Tectonic stress and the spectra of seismic shear waves from earthquakes, *J. Geophys. Res.* **75,** no. 26, 4997–5009, doi: 10.1029/JB075i026p04997.

Bullen, K. E., and B. A. Bolt (1985). *An Introduction to the Theory of Seismology*, Cambridge University Press, Cambridge, United Kingdom, 188–190.

Byerlee, J. (1978). Friction of rocks, *Pure Appl. Geophys.* **116,** 615–626.

Camacho, A., R. H. Vernon, and J. D. Firzgerald (1995). Large volumes of anhydrous pseudotachylyte in the Woodroffe Thrust, eastern Musgrave Ranges, Australia, *J. Struct. Geol.* **17,** 371–383.

Choy, G. L., and V. F. Cormier (1986). Direct measurement of the mantle attenuation operator from broadband P and S waveforms, *J. Geophys. Res.* **91,** 7326–7342.

Clark, D., A. Mcpherson, and T. Allen (2014). Intraplate earthquakes in Australia, in *Intraplate Earthquakes*, P. Talwani (Editor), Cambridge University Press, Cambridge, United Kingdom, 8–49, doi: 10.1017/CBO9781139628921.012.

Clark, D., A. McPherson, and R. Van Dissen (2012). Long-term behaviour of Australian stable continental region (SCR) faults, *Tectonophysics* **566/567,** 1–30, doi: 10.1016/j.tecto.2012.07.004.

Coblentz, D. D., S. Zhou, R. Hillis, R. Richardson, and M. Sandiford (1998). Topography, plate-boundary forces and the Indo-Australian intraplate stress field, *J. Geophys. Res.* **103,** no. B1, 919–931, doi: 10.1029/97JB02381.

Collettini, C., A. Niemeijer, C. Viti, and C. Marone (2009). Fault zone fabric and fault weakness, *Nature* **462,** 907–910.

Copley, A. (2017). The strength of earthquake-generating faults, *J. Geol. Soc.* **175,** no. 1, 1, doi: 10.1144/jgs2017-037.

Copley, A., and N. Woodcock (2016). Estimates of fault strength from the Variscan foreland of the northern UK, *Earth Planet. Sci. Lett.* **451,** 108–113, doi: 10.1016/j.epsl.2016.07.024.

Crotwell, H. P., T. J. Owens, and J. Ritsema (1999). The TauP ToolKit: Flexible seismic travel-time and raypath utilities, *Seismol. Res. Lett.* **70,** no. 2, 154–160, doi: 10.1785/gssrl.70.2.154.

Dawson, J., P. Cummins, P. Tregoning, and M. Leonard (2008). Shallow intraplate earthquakes in Western Australia observed by Interferometric Synthetic Aperture Radar, *J. Geophys. Res.* **113,** no. B11408, doi: 10.1029/2008JB005807.

de Gromard, R. Q., H. M. Howard, R. H. Smithies, M. T. D. Wingate, and Y. Lu (2017). The deep seismic reflection profile 11GA-Y01 in the west Musgrave province: An updated view, *Geol. Surv. Western Australia, Record 2017/8*, 20 pp.

de Gromard, R. Q., C. L. Kirkland, H. M. Howard, M. T. D. Wingate, F. Jourdan, B. I. A. McInnes, M. Danišík, N. J. Evans, B. J. McDonalds, and R. H. Smithies (2019). When will it end, long-lived intracontinental reactivation in central Australia, *Geosci. Front.* **10,** 149–164, doi: 10.1016/j.gsf.2018.09.003.

Di Toro, G., D. L. Goldsby, and T. E. Tullis (2004). Friction falls towards zero in quartz rock as slip velocity approaches seismic rates, *Nature* **427,** 436–439.

Edgoose, C. J., I. R. Scrimgeour, and D. F. Close (2004). *Geology of the Musgrave Block*, Northern Territory Geological Survey, Northern Territory.

Eshelby, J. D. (1957). The determination of the elastic field of an ellipsoidal inclusion, and related problems, *Proc. Roy. Soc. Lon. Math. Phys. Sci.* **241,** no. 1226, 376–396.

Flöttmann, T., M. Hand, D. Close, C. Edgoose, and I. R. Scrimgeour (2004). Thrust tectonic styles of the intracratonic Alice Springs and Petermann orogenies, central Australia, in *Thrust Tectonics and Hydrocarbon Systems*, Vol. 82, K. McClay, and AAPG Mem. (Editors), 538–557.

Freed, A. M. (2005). Earthquake triggering by static, dynamic, and postseismic stress transfer, *Annu. Rev. Earth Planet. Sci.* **33,** 335–367.

Gabrielov, A., V. Keilis-Borok, and D. D. Jackson (1996). Geometric incompatibility in a fault system, *Proc. Natl. Acad. Sci.* **93,** no. 9, 3838–3842.

Gold, R. D., D. Clark, W. D. Barnhart, T. King, M. Quigley, and R. W. Briggs (2019). Surface rupture and distributed deformation revealed by optical satellite imagery: The intraplate 2016 Mw 6.0 Petermann Ranges earthquake, Australia, *Geophys. Res. Lett.* **46,** 10,394–10,403, doi: 10.1029/2019GL084926.

Goldstein, P., D. Dodge, M. Firpo, and L. Minner (2003). SAC2000: Signal processing and analysis tools for seismologists and engineers, in *Invited Contribution to the IASPEI International Handbook of Earthquake and Engineering Seismology*, W. H. K. Lee, H. Kanamori, P. C. Jennings, and C. Kisslinger (Editors), Academic Press, London, United Kingdom, 1613–1614.

Hardebeck, J., and A. Aron (2009). Earthquake stress drops and inferred fault strength on the Hayward Fault, east San Francisco Bay, California, *Bull. Seismol. Soc. Am.* **99,** no. 3, 1801–1814, doi: 10.1785/0120080242.

Hejrani, B., and H. Tkalčić (2019). The 20 May 2016 Petermann Ranges earthquake: centroid location, magnitude, and focal mechanism from full waveform inversion, *Aust. J. Earth Sci.* **66,** no. 1, 37–45, doi: 10.1080/08120099.2018.1525783.

Houston, H., and H. Kanamori (1986). Source spectra of great earthquakes: Teleseismic constraints on rupture process and strong ground motion, *Bull. Seismol. Soc. Am.* **76,** no. 1, 19–42.

Kanamori, H., and G. Stewart (1976). Mode of the strain release along the Gibbs fracture zone, Mid-Atlantic Ridge, *Phys. Earth Planet. In.* **11,** 312–332.

Kaneko, Y., and P. M. Shearer (2014). Seismic source spectra and estimated stress drop derived from cohesive-zone models of circular subshear rupture, *Geophys. J. Int.* **197,** 1002–1015.

King, T. R., M. Quigley, and D. Clark (2018). Earthquake environmental effects produced by the Mw 6.1, 20th May 2016 Petermann earthquake, Australia, *Tectonophysics* **747/748,** 357–372, doi: 10.1016/j.tecto.2018.10.010.

King, T. R., M. Quigley, and D. Clark (2019). Surface-rupturing historical earthquakes in Australia and their environmental effects: New insights from re-analysis of observational data, *Geosciences* **9,** no. 10, **408,** doi: 10.3390/geosciences9100408.

Leonard, M. (2008). One hundred years of earthquake recording in Australia, *Bull. Seismol. Soc. Am.* **98,** 1458–1470, doi: 10.1785/0120050193.

Leonard, M. (2010). Earthquake fault scaling: Self-consistent relating of rupture length, width, average displacement, and moment release, *Bull. Seismol. Soc. Am.* **100,** no. 5A, 1971–1988, doi: 10.1785/0120090189.

Montagner, J. P., and B. L. N. Kennett (1995). How to reconcile body-wave and normal-mode reference Earth models, *Geophys. J. Int.* **125,** 229–248.

Neumann, N. L. (Editor) (2013). *Yilgarn Craton–Officer Basin–Musgrave Province (YOM) Seismic and MT Workshop, Record 2013/28*, Geoscience Australia, Canberra, Australia.

Polcari, M., M. Albano, S. Atzori, C. Bignami, and S. Stramondo (2018). The causative fault of the 2016 M_{wp} 6.1 Petermann Ranges intraplate earthquake (Central Australia) retrieved by C- and L-band InSAR data, *Rem. Sens.* **10,** 1311, doi: 10.3390/rs10081311.

Quigley, M. C., M. L. Cupper, and M. Sandiford (2006). Quaternary faults of south-central Australia: Palaeoseismicity, slip rates and origin, *Aust. J. Earth Sci.* **53,** 285–301, doi: 10.1080/08120090500499271.

Quigley, M. C., A. Jiménez, B. Duffy, and T. R. King (2019). Physical and statistical behaviour of multifault earthquakes, Darfield earthquake case study, New Zealand, *J. Geophys. Res.* **124,** doi: 10.1029/2019JB017508.

Raimondo, T., A. S. Collins, M. Hand, A. Walker-Hallam, R. H. Smithies, P. M. Evins, and H. M. Howard (2010). The anatomy of a deep intracontinental orogen, *Tectonics* **29,** TC4024, doi: 10.1029/2009TC002504.

Rajabi, M., M. Tingay, O. Heidbach, R. Hillis, and S. Renolds (2017). The present-day stress field of Australia, *Earth Sci. Rev.* **168,** 165–189, doi: 10.1016/j.earscirev.2017.04.003.

Salmon, M., B. L. N. Kennett, and E. Saygin (2013). Australian Seismological Reference Model (AuSREM): Crustal component, *Geophys. J. Int.* **192,** 190–206, doi: 10.1093/gji/ggs004.

Sandiford, M. (2002). Low thermal Peclet number intraplate orogeny in central Australia, *Earth Planet. Sci. Lett.* **201,** 309–320.

Scrimgeour, I. R., D. F. Close, and C. J. Edgoose (1999). *Petermann Ranges SG52-7; Explanatory Notes*, Darwin, Australia.

Shea, W. T., Jr., and A. K. Kronenberg (1993). Strength and anisotropy of foliated rocks with varied mica contents, *J. Struct. Geol.* **15,** nos. 9/10, 1097–1121, doi: 10.1016/0191-8141(93)90158-7.

Stewart, A. J. (1995). Western extension of the Woodroffe Thrust, Musgrave Block, central Australia, *J. Aust. Geol. Geophys.* **16,** nos. 1/2, 147–153.

Suppe, J. (2014). Fluid overpressures and strength of the sedimentary upper crust, *J. Struct. Geol.* **69,** no. B, 481–492, doi: 10.1016/j.jsg.2014.07.009.

Talwani, P. (1999). Fault geometry and earthquakes in continental interiors, *Tectonophysics* **305,** 371–379.

Tchalenko, J. S. (1970). Similarities between shear zones of different magnitudes, *Geol. Soc. Am. Bull.* **81,** 1625–1640.

Wang, S., W. Xu, C. Xu, Z. Yin, R. Bürgmann, L. Liu, and G. Jiang (2019). Changes in groundwater level possibly encourage shallow earthquakes in central Australia: The 2016 Petermann Ranges earthquakes, *Geophys. Res. Lett.* **46,** no. 6, 3189–3198, doi: 10.1029/2018GL080510.

Wei, Z., B. L. N. Kennett, and L. F. Zhao (2017). Lg-wave attenuation in the Australian crust, *Tectonophysics* **717,** 413–424.

Wessel, P., W. H. F. Smith, R. Scharroo, J. Luis, and F. Wobbe (2013). Generic mapping tools: Improved version released, *EOS Trans. AGU* **94,** no. 45, 409–410, doi: 10.1002/2013EO450001.

Wex, S., N. S. Mancktelow, A. Camacho, and G. Pennacchioni (2019). Interplay between seismic fracture and aseismic creep in the Woodroffe Thrust, central Australia—Inferences for the rheology of relatively dry continental mid-crustal levels, *Tectonophysics* **758,** 55–72, doi: 10.1016/j.tecto.2018.10.024.

Yifan, Y. (2008). Impact of intensity and loss assessment following the great Wenchuan earthquake, *Earthq. Eng. Eng. Vib.* **7,** 247–254.

Manuscript received 15 October 2019
Published online 12 May 2020